Journal of
Marine Science and Engineering

MDPI

Article

Disturbance Observer-Based Double-Loop Sliding-Mode Control for Trajectory Tracking of Work-Class ROVs

Bolun Huang [1,*] and Qi Yang [1,2]

[1] Collaborative Innovation Center for Advanced Ship and Deep-Sea Exploration, State Key Laboratory of Ocean Engineering, Shanghai Jiao Tong University, Shanghai 200240, China; yangqi110@sjtu.edu.cn
[2] Shanghai Jiao Tong University Underwater Engineering Institute Co., Ltd., Shanghai 200231, China
* Correspondence: huangbolun@sjtu.edu.cn

Abstract: The open-frame structure of work-class ROVs results in significant model uncertainties, and its motion is strongly disturbed by the umbilical cable. To address these problems, this article developed a nonlinear disturbance observer-based super-twisting double-loop sliding-mode control (NDO-STDSMC) method to achieve trajectory tracking control of work-class ROVs with system uncertainties and external disturbances. First, a new outer-loop controller with a novel reaching law is designed to increase the convergence rate compared with the existing double-loop sliding-mode control (DSMC). Second, an inner-loop controller that combines the advantages of the super-twisting sliding-mode scheme is proposed to guarantee the tracking error converges to zero in finite time. Then, a nonlinear disturbance observer is designed to estimate and compensate for the system uncertainties and external disturbances. The stability of the overall control system is proven by the Lyapunov approach. Finally, comprehensive simulation studies on trajectory tracking control of work-class ROVs are provided to demonstrate the efficiency of the proposed NDO-STDSMC method and its superiority over existing DSMC and STDSMC methods.

Keywords: ROVs; disturbance observer; double-loop sliding mode; super-twisting

Citation: Huang, B.; Yang, Q. Disturbance Observer-Based Double-Loop Sliding-Mode Control for Trajectory Tracking of Work-Class ROVs. *J. Mar. Sci. Eng.* **2022**, *10*, 601. https://doi.org/10.3390/jmse10050601

Academic Editor: Claudio Ferrari

Received: 11 March 2022
Accepted: 25 April 2022
Published: 29 April 2022

1. Introduction

Work-class remotely operated vehicles (ROVs) can dive for thousands of meters and perform heavy-duty underwater operations. Through an umbilical cable, ROVs can communicate with surface vehicles in real time. Therefore, they have achieved widespread use in scientific investigations, deep-sea mining, and military affairs, such as for oceanography, bottom surveys, seafloor mapping, deep-sea archaeology, and oil and gas prospecting. Traditional ROVs are manually operated. The human presence makes complex multiobjective underwater missions possible; however, the limitations in sensory feedback to the ROV pilot make certain operations, such as high-precision trajectory tracking, impossible without some form of machine intelligence [1]. Currently, the acute demands for automatic control of ROVs are rapidly increasing; therefore, improving the autonomous capability of ROVs is currently a hot issue [2].

Commonly in practical situations, such as subsea pipeline testing and topographic exploration, ROVs are required to have trajectory tracking capabilities [2]. However, the automatic control of ROVs is never an easy task due to the coupled nonlinearities together with the complex system uncertainties. Moreover, unlike autonomous underwater vehicles (AUVs), a work-class ROV must consider the interference of the umbilical cable. Especially in deep-sea operations, the weight of the umbilical cable will even exceed the weight of the ROV, and the resulting large inertia will cause a strong disturbance to the motion of the ROV. Therefore, it is still a challenge to design a proper control scheme for work-class ROVs to complete trajectory tracking tasks.

Many scholars have devoted themselves to this field to efficiently overcome the aforementioned obstacles and obtain high-precision control performance for ROVs with

uncertain dynamics and external disturbances. Traditional linear controllers, such as proportional–integral–derivative (PID) controllers and linear–quadratic regulators, are often preferred due to their easy implementation [3,4]. However, in the face of highly nonlinear ROV hydrodynamics and, more importantly, very large tether disturbances, their performance degrades significantly, and they cannot provide high-precision motion control capabilities, especially if the desired trajectory represents a curve in the workspace [5]. Therefore, more advanced nonlinear control techniques are resorted to for solving the tracking controller design of ROVs, and these techniques include adaptive-based control [6–9], sliding-mode control (SMC) [10–12], model predictive control (MPC) [13–15], and neural network control [16,17]. SMC is insensitive to model uncertainty and external interference, so it is a powerful, robust control scheme. There are two phases in SMC, namely, the reaching and sliding-mode phases. In the reaching phase, the switching term, which contains the signum function, is used to guarantee that the system state reaches the preset sliding-mode surface. Then, in the sliding-mode phase, the system state repeatedly shuttles over the sliding surface to achieve the robustness requirement. This feature is the source of system robustness, but it also inevitably leads to the chattering problem. In ROV control, this kind of chattering will cause a large thruster force and high-frequency change in speed to meet the output requirements, which will undoubtedly increase energy consumption while increasing the risk of thruster damage. To suppress or eliminate chattering in SMC, some methods, such as the boundary layer method, alternative switching-term method, dynamical gains method, and high-order sliding-mode (HOSM) method, have been proposed [18].

The HOSM method was proposed by Levent et al. Its core idea is to hide the switching term in the integral element to reduce chattering. The HOSM method has been widely used in underwater robots [19–21], UAVs [22,23], robot arms [24,25], and other control and has achieved good results. However, when a large disturbance occurs, the HOSM method still has a chattering problem. Similar to traditional SMC, in the absence of a priori knowledge of external disturbances, a large gain must be employed for the switching term to ensure the robustness of the system, and this approach inevitably leads to an increase in chattering. To overcome the problem of chattering when applying the HOSM method to the control of underwater vehicles, many scholars have proposed their own methods. The authors of [21] proposed a second-order SMC for AUV trajectory tracking. By replacing the discontinuous signum function with a continuous tanh function, the chattering phenomenon was reduced. However, a well-known problem with the substitution function method is that the robustness will be sacrificed when reducing chattering [18]. The authors of [26] proposed a model-free second-order SMC method for ROVs that, in combination with a backpropagation neural network to observe and compensate for the changes in hydrodynamic parameters of ROVs, has shown good results but neglects the influence of the umbilical cable. The authors of [19] proposed a second-order fast nonsingular terminal sliding-mode (FINTSM) method for a fully actuated AUV. Adaptive techniques are utilized to estimate the uncertainties of system parameters so that the switching gain can be selected more purposefully. The FINTSM method can ensure the fast convergence of tracking errors. However, too many parameters need to be set in this method, which is not conducive to practical application.

For work-class ROVs, the umbilical cable will cause a large interference force on ROV motion. Furthermore, the unpredictable currents and complex structures make it difficult to accurately establish a dynamic model of the umbilical cable. Thus, it is hard to describe the accurate real-time cable-generated force acting on an ROV. Therefore, ROV motion control is a typical situation in the absence of a priori knowledge of external disturbances. Direct application of the HOSM method to ROV control will also encounter chattering problems. Some articles have chosen to ignore the effects of the umbilical cable [12,27,28]; however, this is suitable only for small observation-class ROVs and is obviously unrealistic for work-class ROVs.

To deal with the problem of system uncertainties and external disturbances acting on a work-class ROV, it is necessary to employ disturbance suppression methods to enhance the system robustness. An effective alternative method that has emerged in recent years is the application of a disturbance observer (DO). The principle of a DO is to lump the system uncertainties and external disturbances into a single disturbance, and then the lumped disturbance can be estimated and compensated by the designed DO. The combined use of a DO and SMC can also reduce chattering: the lumped disturbance is suppressed by the DO so that the gain of the switching term in SMC can take a smaller value, and the chattering can be reduced as a consequence. Composite control methods based on a DO and SMC have been applied in many aspects, such as in [29–31]. However, in the above articles, the design of the DO is based on an assumption that the lumped disturbance term is slowly time-varying, which satisfies that the first derivative of the disturbance term is equal to zero. In this paper, we propose a nonlinear disturbance observer (NDO) that requires only the derivative of the disturbance to meet the Lipschitz condition (the derivative of the disturbance is bounded), and then the convergence of the observer can be proven.

Inspired by the abovementioned works, we propose a nonlinear disturbance observer-based super-twisting double-loop sliding-mode control (NDO-STDSMC) for the trajectory tracking of work-class ROVs. The proposed method applies the double-loop sliding-mode control (DSMC) structure proposed by [11]; however, novel reaching laws in both the outer and inner loops are proposed, and the positive antidisturbance strategy NDO is introduced in the inner loop to enhance the robustness. Compared with DSMC and STDSMC, our newly proposed NDO-STDSMC has the following advantages: (1) Chattering is further reduced. Combining the advantages of DSMC and ST, the output chattering is further eliminated, and the control accuracy can be effectively ensured. (2) System robustness is enhanced. Thanks to the adoption of a DO, the lumped disturbance can be estimated and compensated. (3) Fast convergence is guaranteed. By integrating a novel reaching law in both the outer and inner loops, the tracking error can be guaranteed to tend to zero with faster convergence.

The remainder of this paper is organized as follows: Section 2 describes the dynamics and kinematics models of work-class ROVs. Section 3 details the design of the controller and the observer and proves the finite-time stability of the system by the Lyapunov approach. In Section 4, a comparative simulation of ROV motion in two typical scenarios is performed to demonstrate the effectiveness and advantages of our newly proposed controller. Finally, some concluding remarks are provided in Section 5.

2. Kinematics and Dynamics Models

The HaiMa ROV shown in Figure 1 is a typical work-class ROV. In general, two coordinate frames, namely, the inertial frame and the body-fixed frame, are usually defined to describe the motion of ROVs. The two coordinate systems are transformed by the Jacobian transformation matrix $\boldsymbol{J}_{\psi}(\boldsymbol{\eta})$:

$$\boldsymbol{J}_{\psi}(\boldsymbol{\eta}) = \begin{bmatrix} \cos\psi & -\sin\psi & 0 & 0 \\ \sin\psi & \cos\psi & 0 & 0 \\ 0 & 0 & 1 & 0 \\ 0 & 0 & 0 & 1 \end{bmatrix} \tag{1}$$

ROV dynamics are based on the following general premises: (1) ROV motion control can be simplified from 6 degrees of freedom (DoFs) to 4 DoFs because ROV roll and pitch are self-stable (metacentric stability) and not driven. In addition, the two uncontrolled DoFs (roll and pitch) span negligibly narrow ranges, so the corresponding dynamics can be omitted [27]. (2) The positions of the center of gravity and the center of buoyancy are fixed. (3) The fluid is irrotational, has constant and uniform density, and has infinite extent.

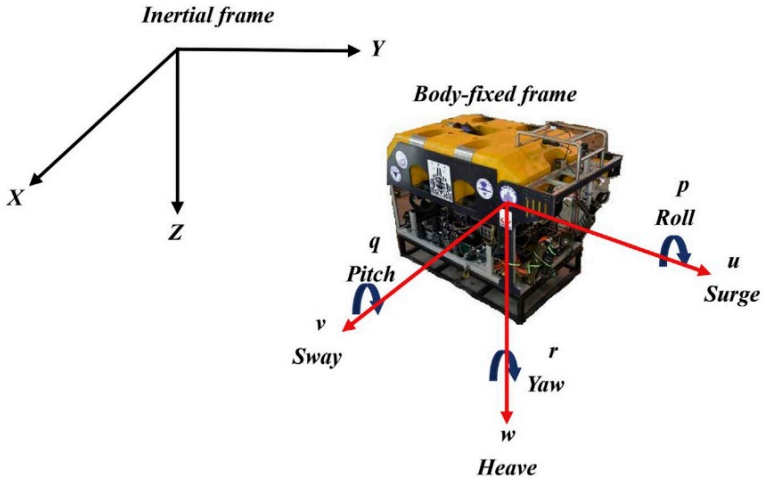

Figure 1. HaiMa ROV.

The kinematics and dynamics models of an ROV can be expressed as:

$$\begin{cases} \dot{\boldsymbol{\eta}} = \boldsymbol{J}_{\psi}(\boldsymbol{\eta})\boldsymbol{v} \\ \boldsymbol{M}\dot{\boldsymbol{v}} + \boldsymbol{C}(\boldsymbol{v})\boldsymbol{v} + \boldsymbol{D}(\boldsymbol{v})\boldsymbol{v} + \boldsymbol{g}(\boldsymbol{\eta}) = \boldsymbol{\tau}_{\mathrm{T}} + \boldsymbol{\tau}_{d} \end{cases} \tag{2}$$

The nomenclature is defined in Table 1.

Table 1. The nomenclature in kinematics and dynamics Models.

Earth-fixed inertial frame	
$\boldsymbol{\eta}^{\mathrm{T}} = [x, y, z, \psi]^{\mathrm{T}}$	ROV position and orientation vector in the yaw plan
Body-fixed frame	
$\boldsymbol{v}^{\mathrm{T}} = [u, v, w, r]^{\mathrm{T}}$	ROV velocity vector in surge, sway, heave, and yaw, respectively
Thrust distribution	
$\boldsymbol{\tau}_{\mathrm{T}} = [\tau_{\mathrm{Tx}}, \tau_{\mathrm{Ty}}, \tau_{\mathrm{Tz}}, \tau_{\mathrm{T\psi}}]^{\mathrm{T}}$ $\boldsymbol{\tau}_{\mathrm{T}} = \boldsymbol{B}_{\mathrm{T}}\boldsymbol{u}$ $\boldsymbol{u} = [u_{\mathrm{T1}}, u_{\mathrm{T2}}, u_{\mathrm{T3}} \cdots u_{\mathrm{T8}}]^{\mathrm{T}}$	The thrust forces and moment acting on the ROV in surge, sway, heave, and yaw, respectively. B_{T} is the thrust distribution matrix, and u is the thrust generated by the eight propellers
Mechanical and hydrodynamic parameters	
$\boldsymbol{M} = diag\{m - X_{\dot{u}}, m - Y_{\dot{v}}, m - Z_{\dot{w}}, I_z - N_{\dot{r}}\}$ $\boldsymbol{C}(\boldsymbol{v}) = \begin{bmatrix} 0 & 0 & 0 & -(m - Y_{\dot{v}})v \\ 0 & 0 & 0 & (m - X_{\dot{u}})u \\ 0 & 0 & 0 & 0 \\ (m - Y_{\dot{v}})v & -(m - X_{\dot{u}})u & 0 & 0 \end{bmatrix}$	m : rigid body mass. I_z : moment of inertia in yaw. $X_{\dot{u}}, Y_{\dot{v}}, Z_{\dot{w}}, \boldsymbol{N}_{\dot{r}}$: added mass and additional inertia
$\boldsymbol{D}(\boldsymbol{v}) = -diag\Big\{X_u + X_{u\lvert u\rvert}\lvert u\rvert, Y_v + Y_{v\lvert v\rvert}\lvert v\rvert, Z_w + Z_{w\lvert w\rvert}\lvert w\rvert, N_r + N_{r\lvert r\rvert}\lvert r\rvert\Big\}$	X_u, Y_v, Z_w, N_r: linear drag coefficient. $X_{u\lvert u\rvert}, Y_{v\lvert v\rvert}, Z_{w\lvert w\rvert}, N_{r\lvert r\rvert}$: quadratic drag coefficient
$\boldsymbol{g}(\boldsymbol{\eta}) = [0, 0, (W - B), 0]^{\mathrm{T}}$	Restoring force matrix, W: weight, B: buoyancy.
$\boldsymbol{\tau}_{\mathrm{L}} = \boldsymbol{\tau}_{ex} + \boldsymbol{\tau}_{su}$	Lumped disturbance, $\boldsymbol{\tau}_{ex}$: external disturbances $\boldsymbol{\tau}_{su}$: system uncertainties

The above hydrodynamic parameters of the "HaiMa" ROV are presented in [11]. However, ROVs are open-frame structures, and their hydrodynamic parameters are easy to change according to changes in motion status and current conditions. This undoubtedly increases the uncertainties of the system. Therefore, each system parameter can be expressed

as the sum of the nominal dynamics $\boldsymbol{M}_0$, $\boldsymbol{C}_0(\boldsymbol{v})$, and $\boldsymbol{D}_0(\boldsymbol{v})$ and dynamic uncertainties $\Delta\boldsymbol{M}$, $\Delta\boldsymbol{C}(\boldsymbol{v})$, and $\Delta\boldsymbol{D}(\boldsymbol{v})$, that is:

$$\boldsymbol{M} = \boldsymbol{M}_0 + \Delta\boldsymbol{M}, \boldsymbol{C}(\boldsymbol{v}) = \boldsymbol{C}_0(\boldsymbol{v}) + \Delta\boldsymbol{C}(\boldsymbol{v}), \boldsymbol{D}(\boldsymbol{v}) = \boldsymbol{D}_0(\boldsymbol{v}) + \Delta\boldsymbol{D}(\boldsymbol{v}), \boldsymbol{g}(\boldsymbol{\eta}) = \boldsymbol{g}_0(\boldsymbol{\eta}) + \Delta\boldsymbol{g}(\boldsymbol{\eta}) \quad (3)$$

Lemma 1. *Assume that V(t) is a continuous positive defined function and that its derivatives satisfy the following inequalities:*

$$\dot{V}(t) + \varepsilon V^{\alpha}(t) \leq 0 \quad (4)$$

where $\varepsilon > 0$ and $0 < \alpha < 1$.

Then, this implies that V(t) will converge to the neighborhood around zero in finite time t_r, which can be expressed as [10]:

$$t_r \leq \ln \frac{V^{1-\alpha}(t_0)}{\varepsilon(1-\alpha)} \quad (5)$$

where $V(t_0)$ is the initial value of $V(x)$.

The control objective of this paper is to design an NDO-STDSMC such that work-class ROVs can achieve trajectory tracking in the presence of strong time-varying external disturbances and system uncertainties. Moreover, the position and attitude tracking errors and sliding surface can be proven to converge to the neighborhood around zero in finite time.

3. Disturbance Observer and Control Strategy Design

In this section, a double-loop control strategy, which is often used in the control of underwater vehicles [11,32–35], is utilized to decompose ROV motion into an inner loop (velocity loop) and an outer loop (position and attitude loop). Controllers are designed separately for the inner and outer loops. The outer-loop controller is combined with a novel reaching law to ensure the fast convergence of the sliding-mode surface while providing the reference velocity to the inner loop. An ST second-order sliding-mode scheme is employed to design the inner-loop controller because of its special ability to remain robust with less chattering [18]. External disturbances and internal uncertainties are estimated and eliminated by the designed nonlinear disturbance observer so that the tracking accuracy and system robustness can be enhanced while the chattering is further reduced. The control strategy diagram is shown in Figure 2.

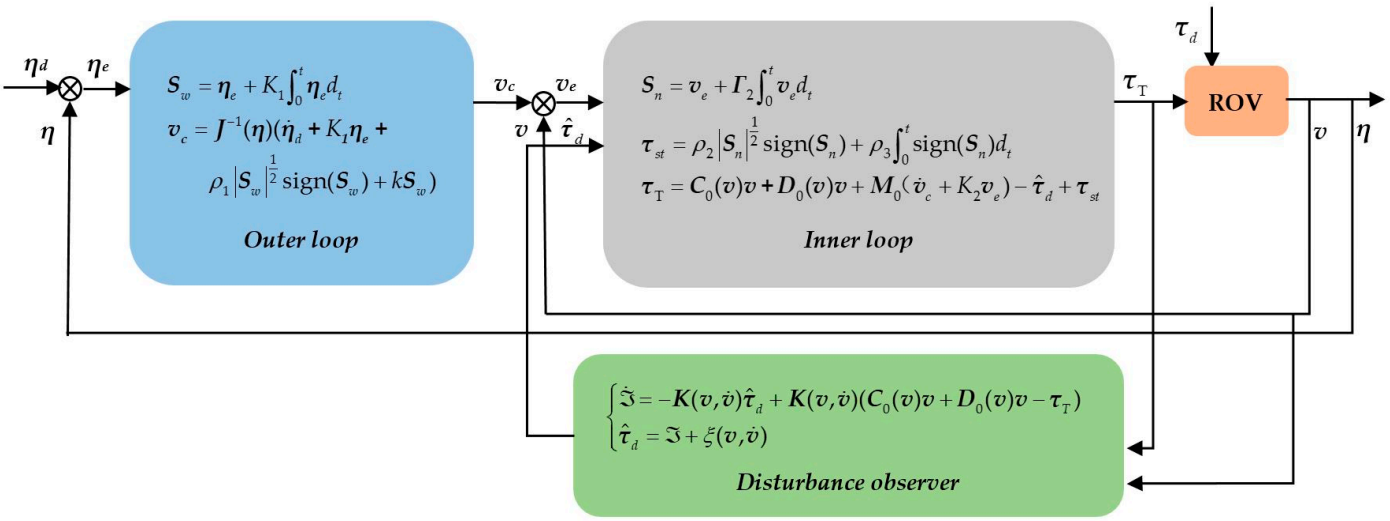

Figure 2. Schematic diagram of NDO-STDSMC.

3.1. Nonlinear Disturbance Observer Design

A conventional disturbance observer (CDO), which is usually used in robotic motion control, is hard to directly apply to an ROV. A CDO can be expressed as:

$$\dot{\hat{\boldsymbol{\tau}}}_L = -\boldsymbol{K}\hat{\boldsymbol{\tau}}_L + \boldsymbol{K}(\boldsymbol{M}_0\dot{\boldsymbol{v}} + \boldsymbol{C}_0(\boldsymbol{v})\boldsymbol{v} + \boldsymbol{D}_0(\boldsymbol{v})\boldsymbol{v} + \boldsymbol{g}_0(\boldsymbol{\eta}) - \boldsymbol{\tau}_{\mathrm{T}}) \tag{6}$$

where $\hat{\boldsymbol{\tau}}_L$ is the estimation of the disturbance $\boldsymbol{\tau}_L$. However, the acceleration $\dot{\boldsymbol{v}}$ is required in (6), but it is hard to obtain the acceleration signal of an ROV. Therefore, we define the following auxiliary functions to design a novel DO:

$$\Im = \hat{\boldsymbol{\tau}}_L - \xi(\boldsymbol{v}, \dot{\boldsymbol{v}}) \tag{7}$$

where auxiliary functions $\xi(\boldsymbol{v}, \dot{\boldsymbol{v}})$ are defined as:

$$\frac{d\xi(\boldsymbol{v}, \dot{\boldsymbol{v}})}{dt} = \boldsymbol{K}(\boldsymbol{v}, \dot{\boldsymbol{v}})\boldsymbol{M}_0\dot{\boldsymbol{v}} \tag{8}$$

where $\boldsymbol{K}(\boldsymbol{v}, \dot{\boldsymbol{v}})$ is the observer gain matrix.

By taking the time derivative of (7) and then substituting (2) and (8) into it, we can obtain:

$$\begin{aligned} \dot{\Im} &= \dot{\hat{\boldsymbol{\tau}}}_L - \boldsymbol{K}(\boldsymbol{v}, \dot{\boldsymbol{v}})\boldsymbol{M}_0\dot{\boldsymbol{v}} \\ &= -\boldsymbol{K}(\boldsymbol{v}, \dot{\boldsymbol{v}})\hat{\boldsymbol{\tau}}_L + \boldsymbol{K}(\boldsymbol{v}, \dot{\boldsymbol{v}})(\boldsymbol{C}_0(\boldsymbol{v})\boldsymbol{v} + \boldsymbol{D}_0(\boldsymbol{v})\boldsymbol{v} + \boldsymbol{g}_0(\boldsymbol{\eta}) - \boldsymbol{\tau}_{\mathrm{T}}) \end{aligned} \tag{9}$$

Therefore, the DO can be designed as:

$$\begin{cases} \dot{\Im} = -\boldsymbol{K}(\boldsymbol{v}, \dot{\boldsymbol{v}})\hat{\boldsymbol{\tau}}_L + \boldsymbol{K}(\boldsymbol{v}, \dot{\boldsymbol{v}})(\boldsymbol{N}_0(\boldsymbol{v}, \boldsymbol{\eta}) - \boldsymbol{\tau}_{\mathrm{T}}) \\ \hat{\boldsymbol{\tau}}_L = \Im + \xi(\boldsymbol{v}, \dot{\boldsymbol{v}}) \end{cases} \tag{10}$$

where $\boldsymbol{N}_0(\boldsymbol{v}, \boldsymbol{\eta}) = \boldsymbol{C}_0(\boldsymbol{v})\boldsymbol{v} + \boldsymbol{D}_0(\boldsymbol{v})\boldsymbol{v} + \boldsymbol{g}_0(\boldsymbol{\eta})$.

Assumption 1. *The derivative of the lumped disturbance term $\dot{\boldsymbol{\tau}}_L$ is continuous and bounded, which means that $\boldsymbol{\tau}_L$ is assumed to be Lipschitz continuous. Hence, there exists an unknown positive constant δ such that $\|\dot{\boldsymbol{\tau}}_d\| \leq \delta$ is satisfied [36].*

Theorem 1. *Define the disturbance tracking error as $\tilde{\boldsymbol{\tau}}_L = \boldsymbol{\tau}_L - \hat{\boldsymbol{\tau}}_L$. Then, the error can be guaranteed globally uniformly ultimately bounded (GUUB) when Assumption 1 is considered.*

Proof of Theorem 1. The Lyapunov function candidate is defined as:

$$V_1 = \frac{1}{2}\tilde{\boldsymbol{\tau}}_L^{\mathrm{T}}\tilde{\boldsymbol{\tau}}_L \tag{11}$$

By taking the derivative of (11), the following can be obtained:

$$\dot{V}_1 = \tilde{\boldsymbol{\tau}}_L^{\mathrm{T}}\dot{\tilde{\boldsymbol{\tau}}}_L = \tilde{\boldsymbol{\tau}}_L^{\mathrm{T}}(\dot{\boldsymbol{\tau}}_L - \dot{\hat{\boldsymbol{\tau}}}_L) \tag{12}$$

By substituting (8) and (10) into (12), it can be deduced that:

$$\begin{aligned} \dot{V}_1 &= \tilde{\boldsymbol{\tau}}_L^{\mathrm{T}}[\dot{\boldsymbol{\tau}}_L - \boldsymbol{K}(\boldsymbol{v}, \dot{\boldsymbol{v}})(\boldsymbol{N}_0(\boldsymbol{v}, \boldsymbol{\eta}) - \boldsymbol{\tau}_{\mathrm{T}}) + \boldsymbol{K}(\boldsymbol{v}, \dot{\boldsymbol{v}})\hat{\boldsymbol{\tau}}_L - \boldsymbol{K}(\boldsymbol{v}, \dot{\boldsymbol{v}})\boldsymbol{M}_0\dot{\boldsymbol{v}}] \\ &= \tilde{\boldsymbol{\tau}}_L^{\mathrm{T}}(\dot{\boldsymbol{\tau}}_L - \boldsymbol{K}(\boldsymbol{v}, \dot{\boldsymbol{v}})\tilde{\boldsymbol{\tau}}_L) \\ &= -\tilde{\boldsymbol{\tau}}_L^{\mathrm{T}}\boldsymbol{K}(\boldsymbol{v}, \dot{\boldsymbol{v}})\tilde{\boldsymbol{\tau}}_L + \tilde{\boldsymbol{\tau}}_L^{\mathrm{T}}\dot{\boldsymbol{\tau}}_L \end{aligned} \tag{13}$$

Using Rayleigh's inequality and considering Assumption 1, the following inequality can be obtained:

$$\begin{gathered} \tilde{\boldsymbol{\tau}}_L^{\mathrm{T}}\boldsymbol{K}(\boldsymbol{v}, \dot{\boldsymbol{v}})\tilde{\boldsymbol{\tau}}_L \geq \lambda_{\min}\big(\boldsymbol{K}(\boldsymbol{v}, \dot{\boldsymbol{v}})\big)\|\tilde{\boldsymbol{\tau}}_L\|^2 \\ \|\tilde{\boldsymbol{\tau}}_L^{\mathrm{T}}\dot{\boldsymbol{\tau}}_L\| \leq \|\tilde{\boldsymbol{\tau}}_L\|\|\dot{\boldsymbol{\tau}}_L\| \leq \|\tilde{\boldsymbol{\tau}}_L\|\delta \end{gathered} \tag{14}$$

where $\lambda_{\min}\left(\boldsymbol{K}(\boldsymbol{v},\dot{\boldsymbol{v}})\right)$ represents the minimum eigenvalue of the matrix $\boldsymbol{K}(\boldsymbol{v},\dot{\boldsymbol{v}})$.

Using Young's inequality, we can obtain:

$$\|\widetilde{\boldsymbol{\tau}}_L\|\delta \leq \frac{\|\widetilde{\boldsymbol{\tau}}_L\|^2+\delta^2}{2} \tag{15}$$

Therefore, (13) can be expressed as:

$$\dot{V}_1 \leq -(2\lambda_{\min}\left(\boldsymbol{K}(\boldsymbol{v},\dot{\boldsymbol{v}})\right)-\frac{1}{2})V_1+\frac{\delta^2}{2} \tag{16}$$

The following is defined: $2\lambda_{\min}\left\{\boldsymbol{K}(\boldsymbol{v},\dot{\boldsymbol{v}})\right\}-\frac{1}{2}=\varpi$

Then, (13) can be rewritten as:

$$\dot{V}_1 \leq -\varpi V_1+\frac{\delta^2}{2} \tag{17}$$

A suitable value of $\boldsymbol{K}(\boldsymbol{v},\dot{\boldsymbol{v}})$ is chosen so that ϖ>0 can be satisfied. Then, according to uniform ultimate boundedness theorems [37], the disturbance tracking error is GUUB. □

3.2. Outer-Loop Controller Design

$\boldsymbol{\eta}_{\mathrm{e}}$ is defined as the tracking error, which can be denoted as $\boldsymbol{\eta}_e=\boldsymbol{\eta}_d-\boldsymbol{\eta}$. The outer-loop sliding-mode surface $\boldsymbol{S}_w$ is defined as the following integral sliding-mode form:

$$\boldsymbol{S}_w=\boldsymbol{\eta}_e+\boldsymbol{\Gamma}_1\int_0^t\boldsymbol{\eta}_e d_t \tag{18}$$

where $\boldsymbol{\Gamma}_1$ represents a positive definite gain vector.

By taking the derivative of (18), the expression can be deduced as:

$$\dot{\boldsymbol{S}}_w=\dot{\boldsymbol{\eta}}_e+\boldsymbol{\Gamma}_1\boldsymbol{\eta}_e=\dot{\boldsymbol{\eta}}_d-\dot{\boldsymbol{\eta}}+\boldsymbol{\Gamma}_1\boldsymbol{\eta}_e \tag{19}$$

Equation (19) does not include $\dot{\boldsymbol{v}}$, so the actual control input $\boldsymbol{\tau}_{\mathrm{T}}$ cannot be obtained. Then, the aim of the outer-loop controller is to generate a reference velocity for the inner-loop controller. $\boldsymbol{v}_c$ is defined as the reference velocity, and $\boldsymbol{v}_e$ is the error between the reference velocity and true velocity.

Substituting $\boldsymbol{v}_e=\boldsymbol{v}_c-\boldsymbol{v}$ and $\dot{\boldsymbol{\eta}}=\boldsymbol{J}_\psi(\boldsymbol{\eta})\boldsymbol{v}$ into (19), we can obtain that:

$$\dot{\boldsymbol{S}}_w=\dot{\boldsymbol{\eta}}_d-\boldsymbol{J}_\psi(\boldsymbol{\eta})(\boldsymbol{v}_c-\boldsymbol{v}_e)+\boldsymbol{\Gamma}_1\boldsymbol{\eta}_e \tag{20}$$

The virtual control input $\boldsymbol{v}_c$ can be designed as:

$$\boldsymbol{v}_c=\boldsymbol{J}_\psi^{-1}(\boldsymbol{\eta})(\dot{\boldsymbol{\eta}}_d+\boldsymbol{K}_1\boldsymbol{\eta}_e+\rho_1|\boldsymbol{S}_w|^{\frac{1}{2}}sign(\boldsymbol{S}_w)+k\boldsymbol{S}_w) \tag{21}$$

where ρ_1 and k are positive definite gains.

Substituting Equation (21) into Equation (20), the derivative of $\boldsymbol{S}_w$ can be rewritten as:

$$\dot{\boldsymbol{S}}_w=-\rho_1|\boldsymbol{S}_w|^{\frac{1}{2}}sign(\boldsymbol{S}_w)-k\boldsymbol{S}_w+\boldsymbol{J}(\boldsymbol{\eta})\boldsymbol{v}_e \tag{22}$$

Theorem 2. *If the virtual control input is designed as Equation (21), then the outer-loop sliding surface $\boldsymbol{S}_w$ will converge to the equilibrium point in finite time with the condition that $\boldsymbol{v}_e \to 0$.*

Proof of Theorem 2. The Lyapunov function candidate is defined as:

$$V_2 = \frac{1}{2} \boldsymbol{S}_w^{\mathrm{T}} \boldsymbol{S}_w \tag{23}$$

By substituting Equation (22) into the derivation of Equation (23), the following can be derived:

$$\begin{aligned} \dot{V}_2 &= \boldsymbol{S}_w^{\mathrm{T}} \dot{\boldsymbol{S}}_w = \boldsymbol{S}_w^{\mathrm{T}} (-\rho_1 |\boldsymbol{S}_w|^{\frac{1}{2}} sign(\boldsymbol{S}_w) - k\boldsymbol{S}_w + \boldsymbol{J}(\boldsymbol{\eta}) \boldsymbol{v}_e) \\ &= \boldsymbol{S}_w^{\mathrm{T}} (-\rho_1 \frac{\boldsymbol{S}_w}{|\boldsymbol{S}_w|^{0.5}} - k\boldsymbol{S}_w + \boldsymbol{J}(\boldsymbol{\eta}) \boldsymbol{v}_e) \\ &\leq -(\mu + k) \|\boldsymbol{S}_w\|^2 + \boldsymbol{S}_w^{\mathrm{T}} \boldsymbol{J}(\boldsymbol{\eta}) \boldsymbol{v}_e \end{aligned} \tag{24}$$

where $\mu = \rho_1 / \left(\sqrt{|\boldsymbol{S}_w|} \right)_{\max}$.

From Equation (24), it can be deduced that $\dot{V}_2$ is negative semidefinite when v_{e} converges to zero. Therefore, the subsystem can be asymptotically stable under the action of Equation (21). □

Remark 1. *The reaching law designed by [11] is that* $\dot{\boldsymbol{S}}_w = -\rho_1 \boldsymbol{S}_w + \boldsymbol{J}(\boldsymbol{\eta}) \boldsymbol{v}_e$. *Obviously, if* $\boldsymbol{v}_e \to 0$ *is satisfied, then* $\boldsymbol{S}_w \to 0$ *when* $t \to \infty$. *This means that the error reaches the sliding-mode surface* $\boldsymbol{S}_w$ *in infinite time. However, the outer-loop controller proposed in this paper can drive the error to converge to the sliding-mode surface in finite time. A brief proof is given below. When* $\boldsymbol{v}_e \to 0$, *we rewrite Equation (22) as:*

$$\dot{\boldsymbol{S}}_w + \rho_1 |\boldsymbol{S}_w|^{\frac{1}{2}} sign(\boldsymbol{S}_w) + k\boldsymbol{S}_w = 0 \tag{25}$$

when $\boldsymbol{S}_w(0) > 0$. *Therefore, Equation (25) can be deduced as:*

$$\dot{\boldsymbol{S}}_w + \rho_1 (\boldsymbol{S}_w)^{\frac{1}{2}} + k\boldsymbol{S}_w = 0 \tag{26}$$

Then, let us define $z = \sqrt{\boldsymbol{S}_w}$, and Equation (26) can be deduced as:

$$2\dot{z} = -\rho_1 - kz \tag{27}$$

By separating variables and integrating both sides, we can obtain:

$$\int_{z(0)}^{0} \frac{-2dz}{\rho_1 + kz} = \int_{0}^{tr} dt \tag{28}$$

Then, we can conclude that:

$$t_r = \frac{2}{k} \ln \frac{\rho_1 + k\sqrt{\boldsymbol{S}_w(0)}}{\rho_1} \tag{29}$$

When $\boldsymbol{S}_w(0) < 0$, we can draw conclusions in the same way. Therefore, the convergence time of the sliding-mode surface $\boldsymbol{S}_w$ is:

$$t_r = \frac{2}{k} \ln \frac{\rho_1 + k\sqrt{|\boldsymbol{S}_w(0)|}}{\rho_1} \tag{30}$$

In the next step, the inner-loop controller is designed as a controller that enables v_e to converge to zero. This will ultimately make the entire system tend to be stable.

3.3. Inner-Loop Controller Design

The inner-loop sliding surface $S_{\mathrm{n}} \in \boldsymbol{R}^{4\times1}$ is also designed as an integral sliding-mode form:

$$\boldsymbol{S}_n = \boldsymbol{v}_e + \boldsymbol{\Gamma}_2 \int_0^t \boldsymbol{v}_e d_t \tag{31}$$

where $\boldsymbol{\Gamma}_2 \in \boldsymbol{R}^{4\times4}$ is a positive definite gain vector. Substituting Equation (2) into Equation (31), the following can be derived:

$$\begin{array}{ll} \dot{\boldsymbol{S}}_n & = \dot{\boldsymbol{v}}_e + \boldsymbol{\Gamma}_2 \boldsymbol{v}_e = \dot{\boldsymbol{v}}_c - \dot{\boldsymbol{v}} + \boldsymbol{\Gamma}_2 \boldsymbol{v}_e \\ & = \dot{\boldsymbol{v}}_c - \boldsymbol{M}_0^{-1}(\boldsymbol{C}_0(\boldsymbol{v})\boldsymbol{v} + \boldsymbol{D}_0(\boldsymbol{v})\boldsymbol{v} - \boldsymbol{\tau}_{\mathrm{T}} - \boldsymbol{\tau}_L) + \boldsymbol{\Gamma}_2 \boldsymbol{v}_e \end{array} \tag{32}$$

The inner-loop control force $\boldsymbol{\tau}_{\mathrm{T}}$ is designed as:

$$\begin{array}{ll} \boldsymbol{\tau}_{\mathrm{T}} = & \boldsymbol{C}_0(\boldsymbol{v})\boldsymbol{v} + \boldsymbol{D}_0(\boldsymbol{v})\boldsymbol{v} - \hat{\boldsymbol{\tau}}_L + \boldsymbol{M}_0[\dot{\boldsymbol{v}}_c + \boldsymbol{\Gamma}_2 \boldsymbol{v}_e \\ & + \rho_2 |\boldsymbol{S}_n|^{\frac{1}{2}} sign(\boldsymbol{S}_n) + \rho_3 \int_0^t sign(\boldsymbol{S}_n) dt)] \end{array} \tag{33}$$

Substituting Equation (33) into Equation (32), we have:

$$\dot{\boldsymbol{S}}_n = -\rho_2 |\boldsymbol{S}_n|^{\frac{1}{2}} sign(\boldsymbol{S}_n) - \rho_3 \int_0^t sign(\boldsymbol{S}_n) dt + \boldsymbol{M}_0^{-1} \tilde{\boldsymbol{\tau}}_L \tag{34}$$

Theorem 3. *Under the action of Equation (33), the inner-loop system can achieve stability in finite time.*

Proof of Theorem 3. Define $\Re_1 \in \mathrm{R}^{4\times1}$ and $\Re_2 \in \mathrm{R}^{4\times1}$ as:

$$\begin{cases} \Re_1 = \boldsymbol{S}_n \\ \Re_2 = -\rho_3 \int_0^t sign(\boldsymbol{S}_n) dt) + \boldsymbol{M}_0^{-1} \tilde{\boldsymbol{\tau}}_d \end{cases} \tag{35}$$

Then, considering Equation (34), the derivation of Equation (35) can be deduced as:

$$\begin{cases} \dot{\Re}_1 = -\rho_2 |\Re_1|^{\frac{1}{2}} sign(\Re_1) + \Re_2 \\ \dot{\Re}_2 = -\rho_3 sign(\Re_1) + \boldsymbol{M}_0^{-1} \dot{\tilde{\boldsymbol{\tau}}}_L \end{cases} \tag{36}$$

Define a new vector $\boldsymbol{\sigma} \in \mathrm{R}^{8\times1}$ as follows:

$$\boldsymbol{\sigma} = \begin{bmatrix} \sigma_1 & \sigma_2 \end{bmatrix}^{\mathrm{T}} = \begin{bmatrix} |\Re_1|^{\frac{1}{2}} sign(\Re_1) & \Re_2 \end{bmatrix}^{\mathrm{T}} \tag{37}$$

We can deduce that:

$$\dot{\boldsymbol{\sigma}} = \frac{1}{|\Re_1|^{0.5}} \left(\boldsymbol{A}\boldsymbol{\sigma} + \boldsymbol{B}\boldsymbol{\gamma} |\Re_1|^{0.5} \right) \tag{38}$$

where matrices $\boldsymbol{A} \in \mathrm{R}^{2\times2}$, $\boldsymbol{B} \in \mathrm{R}^{2\times2}$, and $\boldsymbol{\gamma} \in \mathrm{R}^{4\times1}$ can be written as:

$$\boldsymbol{A} = \begin{bmatrix} -\frac{1}{2}\rho_2 & \frac{1}{2} \\ -\rho_3 & 0 \end{bmatrix}, \boldsymbol{B} = \begin{bmatrix} 0 \\ 1 \end{bmatrix}, \boldsymbol{\gamma} = \frac{1}{2} \boldsymbol{M}_0^{-1} \dot{\tilde{\boldsymbol{\tau}}}_d \tag{39}$$

According to the previous proof, $\boldsymbol{\gamma}$ is obviously bounded, which satisfies $\|\boldsymbol{\gamma}\| \leq \omega$, ω>0. For a symmetric positive definite matrix $\boldsymbol{P}$, such as:

$$\boldsymbol{P} = \begin{bmatrix} p_1 & p_2 \\ p_2 & p_3 \end{bmatrix}$$

where p_1 and p_3 are positive definite and $p_1 p_3 > p_2^2$.

We can find a positive definite matrix $\boldsymbol{Q}$ that satisfies the following equality:

$$\boldsymbol{A}^{\mathrm{T}}\boldsymbol{P}+\boldsymbol{P}\boldsymbol{A}+\delta^{2}\boldsymbol{C}+\boldsymbol{P}\boldsymbol{B}\boldsymbol{B}^{\mathrm{T}}\boldsymbol{P}=-\boldsymbol{Q} \tag{40}$$

where $\boldsymbol{C}=\begin{bmatrix}1&0\\0&0\end{bmatrix}$.

The following Lyapunov function candidate is defined as:

$$V_3=\boldsymbol{\sigma}^{\mathrm{T}}\boldsymbol{P}\boldsymbol{\sigma} \tag{41}$$

By taking the derivative of Equation (46) and substituting it into Equation (43):

$$\begin{aligned}\dot{V}_3&=\dot{\boldsymbol{\sigma}}^{\mathrm{T}}\boldsymbol{P}\boldsymbol{\sigma}+\boldsymbol{\sigma}^{\mathrm{T}}\boldsymbol{P}\dot{\boldsymbol{\sigma}}\\&=\tfrac{1}{|\Re_1|^{\frac{1}{2}}}\left[\left(\boldsymbol{A}\boldsymbol{\sigma}+\boldsymbol{B}\boldsymbol{\gamma}|\Re_1|^{\frac{1}{2}}\right)^{\mathrm{T}}\boldsymbol{P}\boldsymbol{\sigma}+\boldsymbol{\sigma}^{\mathrm{T}}\boldsymbol{P}\left(\boldsymbol{A}\boldsymbol{\sigma}+\boldsymbol{B}\boldsymbol{\gamma}|\Re_1|^{\frac{1}{2}}\right)\right]\\&=\tfrac{1}{|\Re_1|^{\frac{1}{2}}}\left[\boldsymbol{\sigma}^{\mathrm{T}}\left(\boldsymbol{A}^{\mathrm{T}}\boldsymbol{P}+\boldsymbol{P}\boldsymbol{A}\right)\boldsymbol{\sigma}+2|\Re_1|^{\frac{1}{2}}(\boldsymbol{B}\boldsymbol{\gamma})^{\mathrm{T}}\boldsymbol{P}\boldsymbol{\sigma}\right]\end{aligned} \tag{42}$$

Considering that the time derivative of σ_1 can be expressed as:

$$\dot{\sigma}_1=\frac{1}{2|\Re_1|^{\frac{1}{2}}}\dot{\Re}_1 \tag{43}$$

Since $|\sigma_1|=|\Re_1|^{\frac{1}{2}}$, substituting Equation (48) into Equation (47) leads to:

$$\dot{V}_3=\frac{1}{|\sigma_1|}\left[\boldsymbol{\sigma}^{\mathrm{T}}\left(\boldsymbol{A}^{\mathrm{T}}\boldsymbol{P}+\boldsymbol{P}\boldsymbol{A}\right)\boldsymbol{\sigma}+2|\sigma_1|(\boldsymbol{B}\boldsymbol{\gamma})^{\mathrm{T}}\boldsymbol{P}\boldsymbol{\sigma}\right] \tag{44}$$

Then, applying Young's inequality, we can obtain:

$$\begin{aligned}2|\sigma_1|(\boldsymbol{B}\boldsymbol{\gamma})^{\mathrm{T}}\boldsymbol{P}\boldsymbol{\sigma}&\leq\gamma^{2}|\sigma_1|^{2}+\boldsymbol{\sigma}^{\mathrm{T}}\boldsymbol{P}\boldsymbol{B}\boldsymbol{B}^{\mathrm{T}}\boldsymbol{P}\boldsymbol{\sigma}\\&\leq\mu^{2}\boldsymbol{\sigma}^{\mathrm{T}}\boldsymbol{C}\boldsymbol{\sigma}+\boldsymbol{\sigma}^{\mathrm{T}}\boldsymbol{P}\boldsymbol{B}\boldsymbol{B}^{\mathrm{T}}\boldsymbol{P}\boldsymbol{\sigma}\end{aligned} \tag{45}$$

By considering Equation (40) and then substituting Equation (45) into Equation (44), it can be deduced that:

$$\begin{aligned}\dot{V}_3&\leq\tfrac{1}{|\sigma_1|}\left(\boldsymbol{\sigma}^{\mathrm{T}}\left(\boldsymbol{A}^{\mathrm{T}}\boldsymbol{P}+\boldsymbol{P}\boldsymbol{A}\right)\boldsymbol{\sigma}+\mu^{2}\boldsymbol{\sigma}^{\mathrm{T}}\boldsymbol{C}\boldsymbol{\sigma}+\boldsymbol{\sigma}^{\mathrm{T}}\boldsymbol{P}\boldsymbol{B}\boldsymbol{B}^{\mathrm{T}}\boldsymbol{P}\boldsymbol{\sigma}\right)\\&=\tfrac{1}{|\sigma_1|}\left[\boldsymbol{\sigma}^{\mathrm{T}}\left(\boldsymbol{A}^{\mathrm{T}}\boldsymbol{P}+\boldsymbol{P}\boldsymbol{A}+\mu^{2}\boldsymbol{\sigma}^{\mathrm{T}}\boldsymbol{C}\boldsymbol{\sigma}+\boldsymbol{\sigma}^{\mathrm{T}}\boldsymbol{P}\boldsymbol{B}\boldsymbol{B}^{\mathrm{T}}\boldsymbol{P}\right)\boldsymbol{\sigma}\right]\\&=-\tfrac{1}{|\sigma_1|}\boldsymbol{\sigma}^{\mathrm{T}}\boldsymbol{Q}\boldsymbol{\sigma}\end{aligned} \tag{46}$$

It follows from Rayleigh's inequality that:

$$\begin{aligned}V_3&<\lambda_{\max}(\boldsymbol{P})\|\boldsymbol{\sigma}\|^{2}<\lambda_{\max}(\boldsymbol{P})|\sigma_1|^{2}\\\dot{V}_3&<-\tfrac{\lambda_{\min}(\boldsymbol{Q})}{|\sigma_1|}\|\boldsymbol{\sigma}\|^{2}<-\lambda_{\min}(\boldsymbol{Q})|\sigma_1|\end{aligned} \tag{47}$$

where $\lambda_{\min}(\cdot)$ represents the minimum eigenvalue of the matrix.

Therefore, we can obtain:

$$\dot{V}_3<-\frac{\lambda_{\min}(\boldsymbol{Q})}{\sqrt{\lambda_{\max}(\boldsymbol{P})}}\sqrt{V_3} \tag{48}$$

It can be concluded that V_3 is positive definite, while its derivative $\dot{V}_3$ is negative definite, and the inner-loop system can be guaranteed to be stable. Furthermore, according to Lemma 1, the tracking error can achieve finite-time convergence. □

According to the above stability proofs of both the inner and outer loops, if the inner-loop gain $\boldsymbol{\Gamma}_2$ is selected to be much larger than the outer-loop gain $\boldsymbol{\Gamma}_1$, then the convergence speed of the inner loop will be greater than that of the outer loop. Therefore, the stability of the overall system can be guaranteed.

4. Numerical Simulation Results

This section illustrates the efficacy of the proposed NDO-STDSMC scheme and its advantages over the DSMC and STDSMC schemes. Comparative simulations employing the realistic dynamics of the HaiMa ROV under the effects of internal uncertainties and unknown external disturbances are carried out to demonstrate the effectiveness.

Work-class ROVs use hydraulic propellers. The thrust and speed of each thruster are limited, so the thrust saturation must be considered. The thrust limits of the "HaiMa" ROV are as follows: the thrust limits of the four horizontal thrusters are 355 kgf to −296 kgf (3481.4 N to −2902.8 N), and the thrust limits of the four vertical thrusters are 198 kgf to −176 kgf (1941.7 N to −1726.0 N).

There are two ways to assemble the umbilical cable of a work-class ROV, as shown in Figure 3.

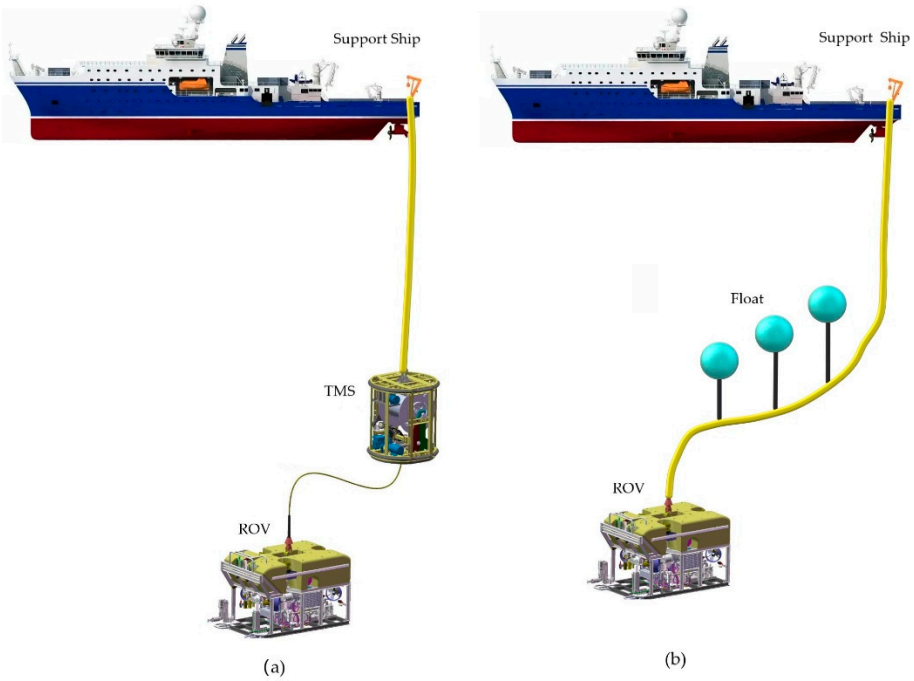

Figure 3. Two operation modes of ROVs: (**a**) ROV with TMS; (**b**) ROV without TMS.

Figure 3a shows an ROV with a tether management system (TMS). The primary cable connects the TMS and the support ship and has a larger diameter and greater bending stiffness. The secondary cable connecting the TMS and ROV can be regarded as a flexible cable with less rigidity. The introduction of a TMS can effectively reduce the effect of the cable on ROV movement. However, the TMS structure introduces more joints and connectors to the system, which are prone to mechanical and electrical failures. An ROV without a TMS, as shown in Figure 3b, is more flexible in deployment, but the ROV motion is also more affected by umbilical cables. Generally, some floating balls are tied at the end near the ROV, or self-floating cables are used to generate buoyancy, which can lightly reduce the interference of the cables on the ROV movement.

To ensure the universality of the controller, ROVs of these two modes are simulated in this paper. The main difference between the two modes is the disturbance force generated by the umbilical cable on the ROV. For the mode with a TMS, the flexible umbilical cable dynamic model proposed in [38] is adopted in this paper because the ROV mentioned in that paper has a similar size and weight than those in this paper, and the model has

been experimentally verified. For the case without a TMS, a model that can accurately describe the dynamic characteristics of the umbilical cable has rarely been found, and most papers use static analysis of the cable. Therefore, this paper adopts a general mode that can simulate the disturbance force acting on work-class ROVs, similar to [39]; that is, the lumped disturbance force is described as a time-varying function. In contrast to the above articles with relatively small disturbances, the peak force of the disturbance force selected in this paper is approximately 5000 N, which can be used to simulate situations that will actually happen for work-class ROVs. The instantaneous disturbance force is greater than the maximum thrusts of the thrusters, which can lead to ROVs being almost out of control.

Considering that an ROV's open-frame structure causes large model uncertainties, 20% uncertainties are added to each hydrodynamic parameter during the simulation process. The nominal hydrodynamic parameters of the "HaiMa" ROV are listed in [11] and are not repeated here.

To showcase the efficacy, a comparison of the proposed NDO-STDSMC is made with DSMC and STDSMC under two modes. Both DSMC and STDSMC were designed for a complete 6-DoF nonlinear model of the "HaiMa" ROV without decoupling the dynamics. To illustrate the overall performance improvement of the inner- and outer-loop controllers proposed in this paper, the DSMC method uses the same controller design as [11]. For STDSMC, the outer-loop and inner-loop controllers are chosen to be the same as those proposed in this paper but without the DO. The comparison results of the three control schemes are demonstrated in the following subsections.

4.1. Scenario A: The ROV with a TMS

In this case, the process of autonomously completing a seabed map scan by the ROV is simulated. The composite trajectory includes the linear motion, yaw motion, and fixed-height motion of the ROV. The desired trajectory in the inertial frame is described as follows:

$$x_d(t) = \begin{cases} 0.5t\ m,\ 0 \le t<40\ s \\ 20\ m,\ 40 \le t < 60\ s \\ 20 - 0.5(t-60)\ m,\ 60 \le t < 100\ s \\ 0\ m,\ 100 \le t < 120\ s \\ 0.5(t-120)\ m,\ 120 \le t \le 160\ s \end{cases}$$

$$y_d(t) = \begin{cases} 10\ m,\ 0 \le t<40\ s \\ 10 - 0.5(t-40)\ m,\ 40 \le t < 60\ s \\ 0\ m,\ 60 \le t < 100\ s \\ -0.5(t-100)\ m,\ 100 \le t < 120\ s \\ -10\ m,\ 120 \le t \le 160\ s \end{cases}$$

$$z_d(t) = 5 - 4\cos(0.1\pi) + 5\sin(0.1\pi x) + 4\cos(0.1\pi y)\ m$$

$$\psi_d(t) = \begin{cases} 0\ rad,\ 0 \le t<40\ s \\ -\pi/2\ rad,\ 40 \le t < 60\ s \\ -\pi\ rad,\ 60 \le t < 100\ s \\ -\pi/2\ rad,\ 100 \le t < 120\ s \\ 0\ rad,\ 120 \le t \le 160\ s \end{cases}$$

For the three control schemes, the initial position and attitude are set as $\boldsymbol{\eta}_0$ = (0 m 9 m 9 m 0 rad 0 rad 0 rad). The initial velocities of the ROV are defined as zero at the initial time t = 0 s.

In this mode, the dynamic model of the disturbance force generated by the umbilical cable can be described as [38]:

$$\boldsymbol{\tau}_d = \begin{cases} f_X = & -942 - 3.0429X - 0.1314Y^2 - 0.225Z^2 - 28.4706Z \\ f_Y = & -8.2134Y \\ f_Z = & -450 - 0.0684X^2 + 4.7493X \\ & -0.1125Y^2 - 0.693Z^2 - 33.2529Z \\ \boldsymbol{M}_\psi = & (fx + fy + fz) \times 0.1 \end{cases}$$

To ensure the fairness of the comparison, the same control parameter values are used in the three controllers. However, in the inner loop, due to the introduction of the DO, the value of ρ_2 in NDO-STDSMC can be taken as smaller than that in the other two controllers. The relevant parameters in the three controllers are selected as Table 2:

Table 2. Controller parameters used in the simulations.

Controller	Parameter Values
DSMC	Γ_1 = diag(0.3,0.3,0.3,0.3) Γ_2 = diag(3,3,3,3) ρ_1 = 0.1 ρ_3 = 0.01
STDSMC	Γ_1 = diag(0.3,0.3,0.3,0.3) Γ_2 = diag(3,3,3,3) ρ_1 = 0.1 ρ_2 = 0.15 ρ_3 = 0.01 k = 1
NDO-STDSMC	Γ_1 = diag(0.3,0.3,0.3,0.3) Γ_2 = diag(3,3,3,3) ρ_1 = 0.1 ρ_2 = 0.036 ρ_3 = 0.0005 k = 1 K = diag(30,30,30,30)

The 3-D and plan views of the ROV trajectory tracking under the three controllers are shown in Figure 4. The tracking errors of each direction are illustrated in Figure 5.

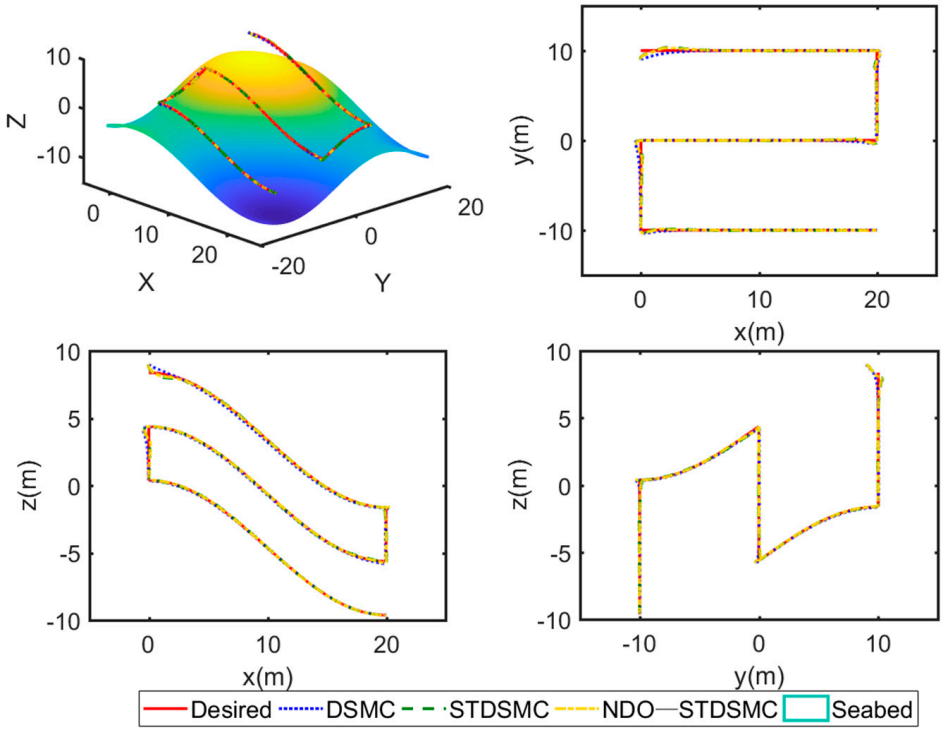

Figure 4. Trajectory tracking results of the ROV associated with the three different controllers in simulation A.

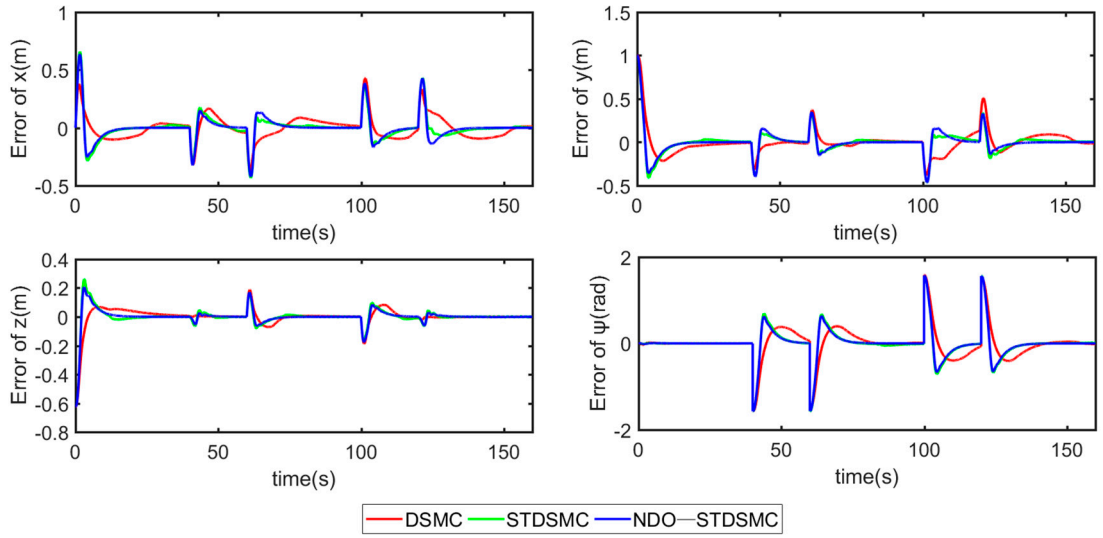

Figure 5. Tracking errors for the position and attitude of the ROV associated with the three controllers in simulation A.

As illustrated in Figure 4, the ROV can achieve proper trajectory tracking under the action of all three controllers. However, as shown in Figure 5, the difference in accuracy among the three controllers is obviously revealed. It can be concluded that the control accuracy of the DSMC method is markedly inferior to that of the other two methods. This is because the convergence speed of the outer-loop controller adopted by the DSMC method is significantly slower than that of the other two methods, which leads to slower convergence of the tracking error under the time-varying target path. To provide a more direct numerical comparison, the mean and root mean square error (RMSE) of the tracking errors in each direction are listed in Table 3.

Table 3. Performance comparison of simulation A.

Performance Comparison	DSMC	STDSMC	NDO-STDSMC
		MEAN	
x	0.07458	-1.9×10^{-5}	3.8×10^{-4}
y	0.00262	5.1×10^{-4}	5.0×10^{-5}
z	0.01038	1.5×10^{-5}	9.4×10^{-6}
ψ	0.03401	-1.8×10^{-3}	-6.0×10^{-4}
		RMSE	
x	0.09305	0.11010	0.10560
y	0.14900	0.13340	0.13080
z	0.07489	0.06768	0.06355
ψ	0.39730	0.34430	0.33500

As shown in this table, the tracking errors of the STDSMC and NDO-STDSMC methods are significantly smaller than those of the DSMC method. Additionally, except that the average value of the tracking error in the x direction of the NDO-STDSMC method is slightly larger than that of the STDSMC method, the errors in the other directions are smaller. This shows that the introduction of the DO enhances the robustness and stability of the controller. Figure 6 shows that the observer can estimate the lumped disturbance force very accurately in this scenario.

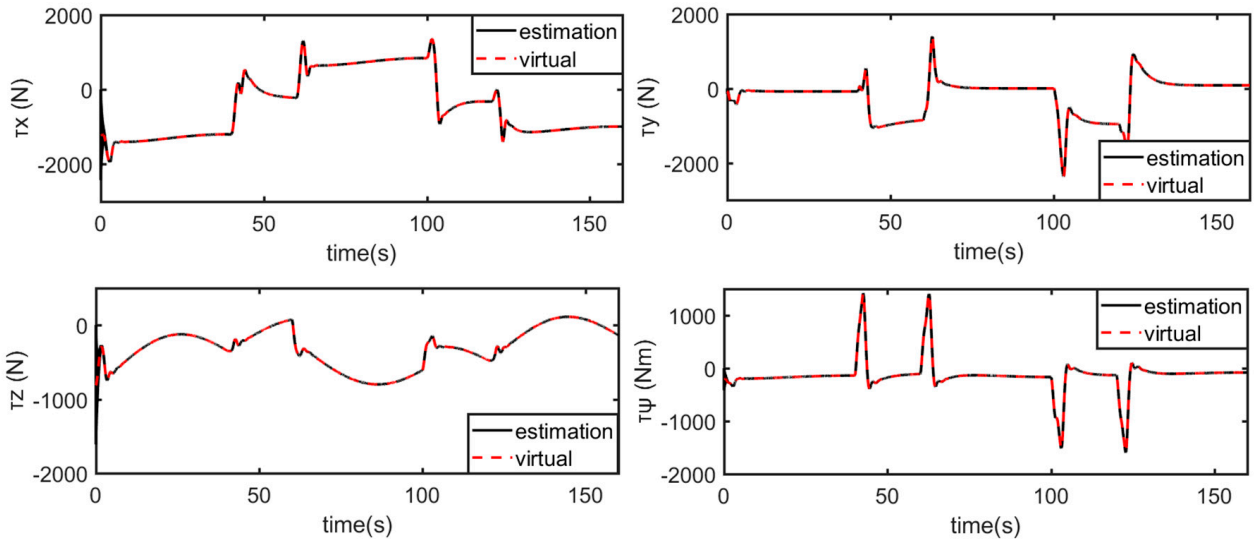

Figure 6. Observation of the lumped disturbance in simulation A.

Figure 7 shows the output of the eight thrusters of the three controllers. It can be seen from the figure that at the time when the target path changes, such as 40, 60, 100, and 120 s, there is unavoidable chattering in all three methods. During the period when the path is stable, such as 70 to 90 s, the NDO-STDSMC method exhibits almost no chattering, while the DSMC and STDSMC methods exhibit more obvious chattering. This shows that the proposed controller can significantly suppress the output chattering while ensuring stability and robustness, which is more suitable for practical applications.

4.2. Scenario B: The ROV without a TMS

In this mode, the efficacy and advantages of the proposed controller are tested by tracking a desired trajectory given in [11], which contains common operating conditions for ROV operations, such as a fixed depth, fixed height, and fixed yaw angle. The lumped environmental and cable disturbances made up of sine functions are considered as follows:

$$\boldsymbol{\tau}_u = \begin{cases} \tau_{dx} = 5000sin(0.2t)\ N \\ \tau_{dy} = 5000sin(0.3t)\ N \\ \tau_{dz} = 5000sin(0.1t)\ N \\ \tau_{dr} = 5000sin(0.2t)\ N{\cdot}m \end{cases}$$

The parameters of the three controllers are the same as those in scenario A.

Figure 8 gives the 3-D and plan views of the ROV trajectory tracking under the three control methods. Figure 9 shows the corresponding position and attitude tracking errors in each direction. From Figures 8 and 9, the tracking accuracy of Scenario B is significantly lower than that of Scenario A, and the statistics in Table 4 can also support this view. This is because the disturbance set in Scenario B is very large, and even exceeds the thrust of a single propeller at some moments, which can be reflected from Thrusts 1 to 5 in Figure 10. Therefore, the huge disturbance poses a great challenge to the robustness of the controller. Without the support of ST and DO technology, the DSMC method has a large gap in stability and robustness with the other two methods. The NDO-STDSMC method improves the robustness and tracking accuracy more significantly than STDSMC, which can be concluded by the numerical comparison in Table 4.

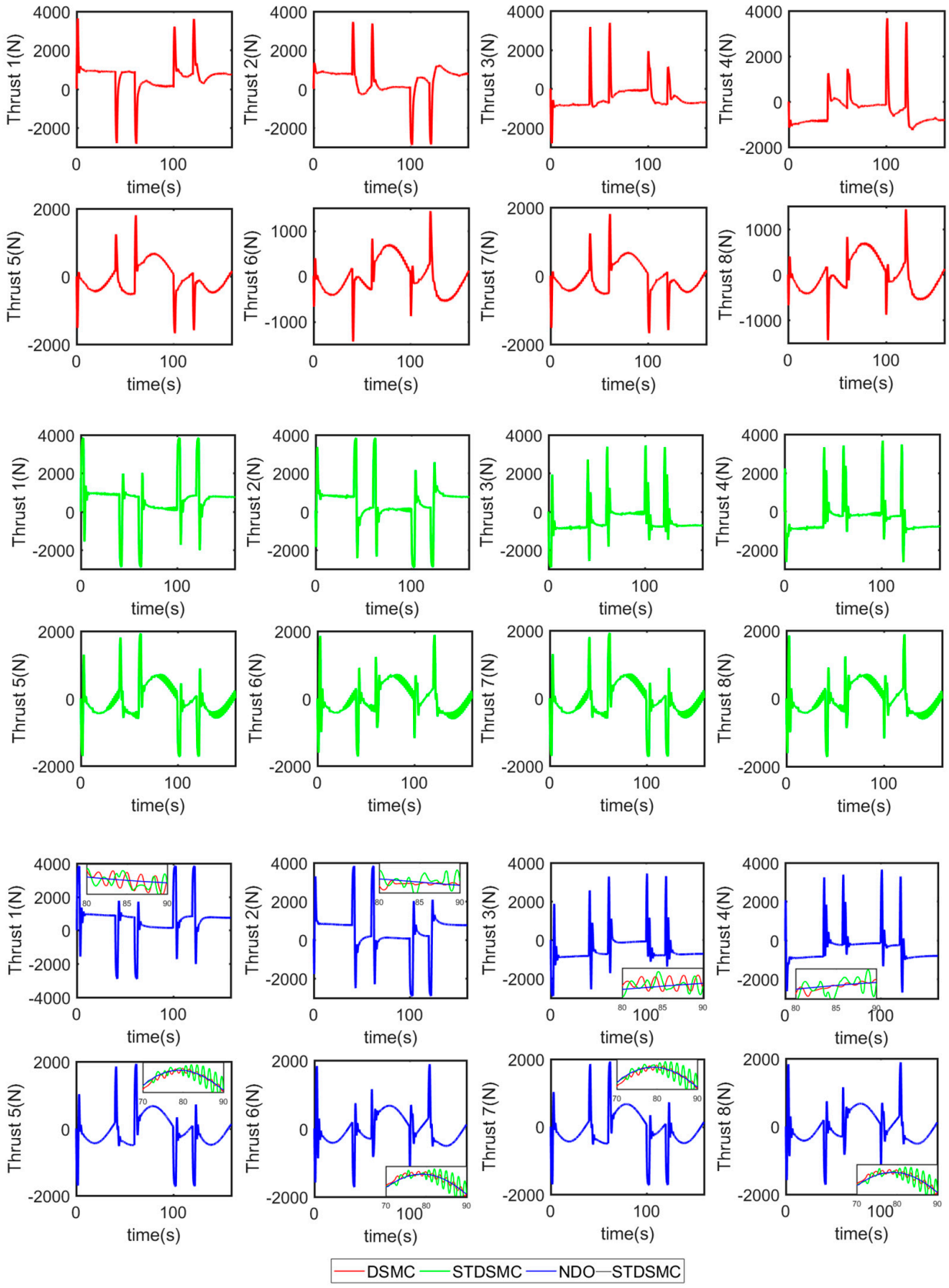

Figure 7. Thrust force for each thruster of the ROV under the action of the three controllers in simulation A.

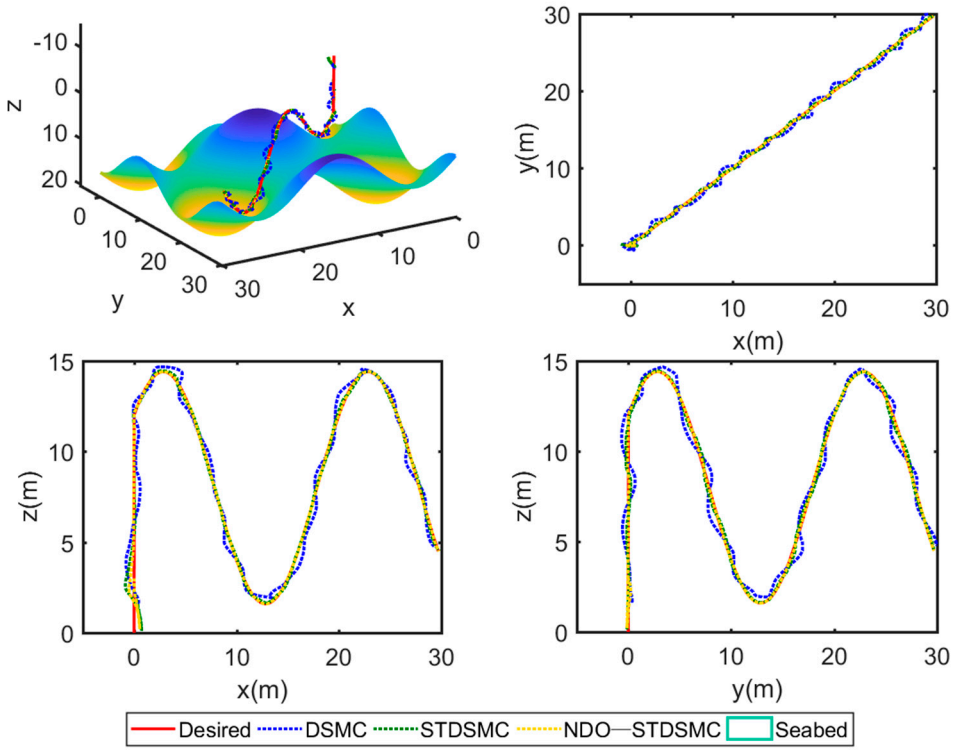

Figure 8. Trajectory tracking results of the ROV associated with the three different controllers in simulation B.

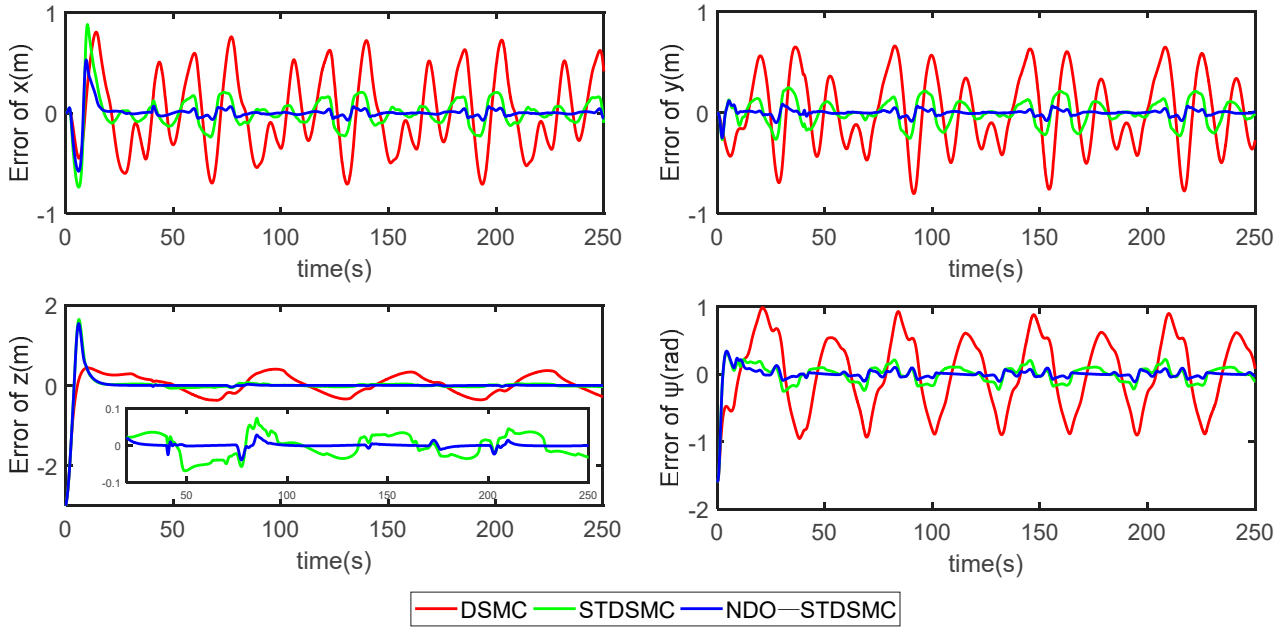

Figure 9. Tracking errors for the position and attitude of the ROV associated with the three controllers in simulation B.

Table 4. Performance comparison of simulation B.

Performance Comparison	DSMC	STDSMC	NDO-STDSMC
	MEAN		
x	0.01326	0.00164	-6.62×10^{-5}
y	-0.00266	-1.3×10^{-4}	-8.2×10^{-5}
z	0.01254	-4.0×10^{-4}	-5.1×10^{-5}
ψ	0.02254	-3.3×10^{-4}	-1.6×10^{-4}
	RMSE		
x	0.3966	0.08746	0.02064
y	0.3923	0.09098	0.02387
z	0.3469	0.30040	0.29300
ψ	0.4604	0.13450	0.12310

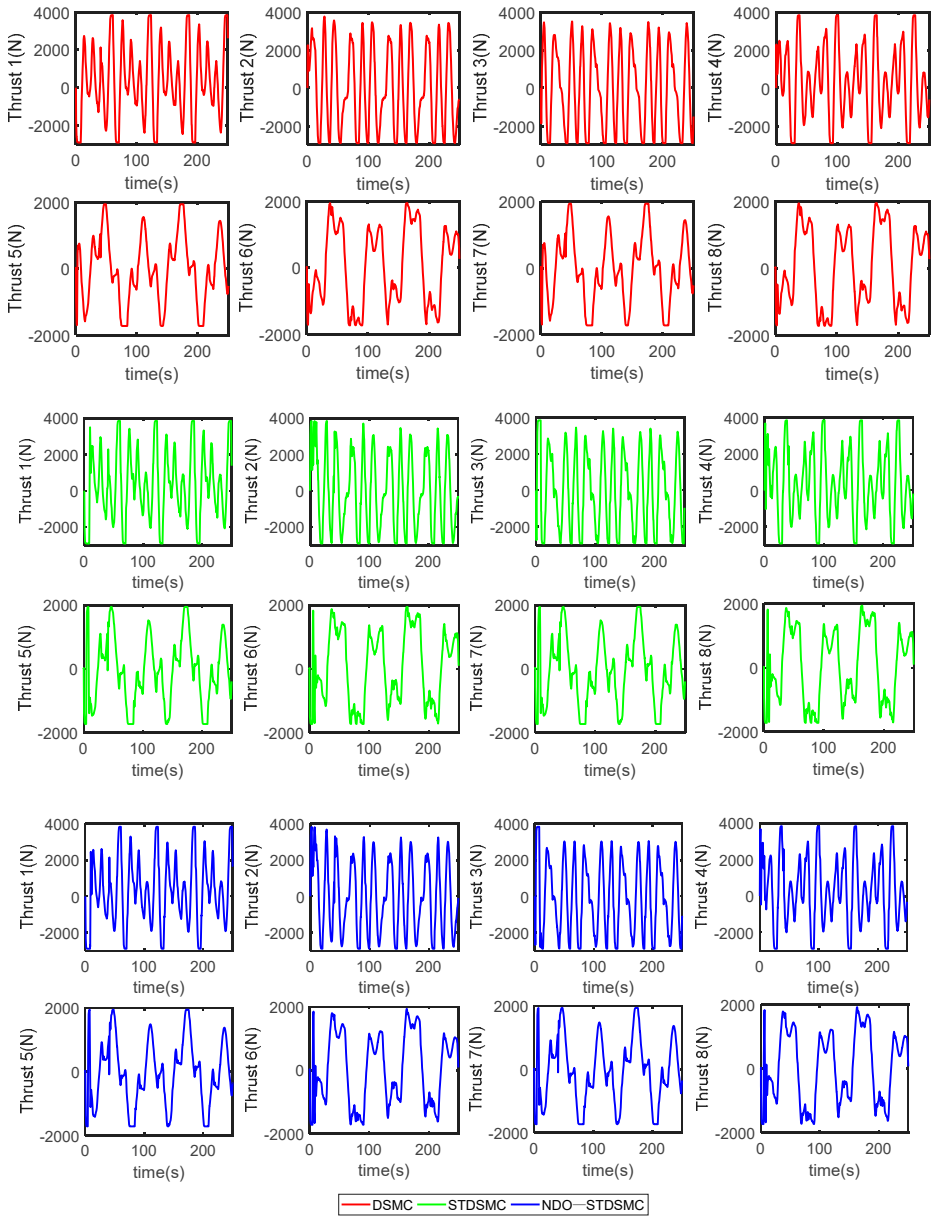

Figure 10. Thrust force for each thruster of the ROV under the action of the three controllers in simulation B.

Figure 10 depicts the thrust forces of the ROV's eight thrusters under the three controllers. This figure shows that the chattering is almost the same for the three controllers, chattering inevitably occurs at the nonsmooth trajectory transition instants, and there is almost no chattering in other consecutive stages. This shows that the NDO-STDSMC method does not improve the control accuracy and robustness at the cost of increasing the chattering. Due to the large external disturbances, some thrusters have short-term output saturation, which is often encountered in the actual operation of ROVs in large depth.

The advantages of NDO-STDSMC are due to the utilization of the NDO because the strong external disturbances are accurately estimated by the observer. Different from the passive antidisturbance methods of DSMC and STDSMC, the introduction of the NDO is a feedforward compensation for the control system, which is an active antidisturbance strategy. Figure 11 shows the actual disturbances and their estimates in each direction of the ROV motion. It is clear that the estimates of the NDO are very accurate. The observer compensates for the influence of external interference on the ROV motion, so the control system can achieve more robustness, thereby ensuring more accurate trajectory tracking. This again illustrates that when large disturbances exist, using a DO is an effective way to improve the robustness of the controller.

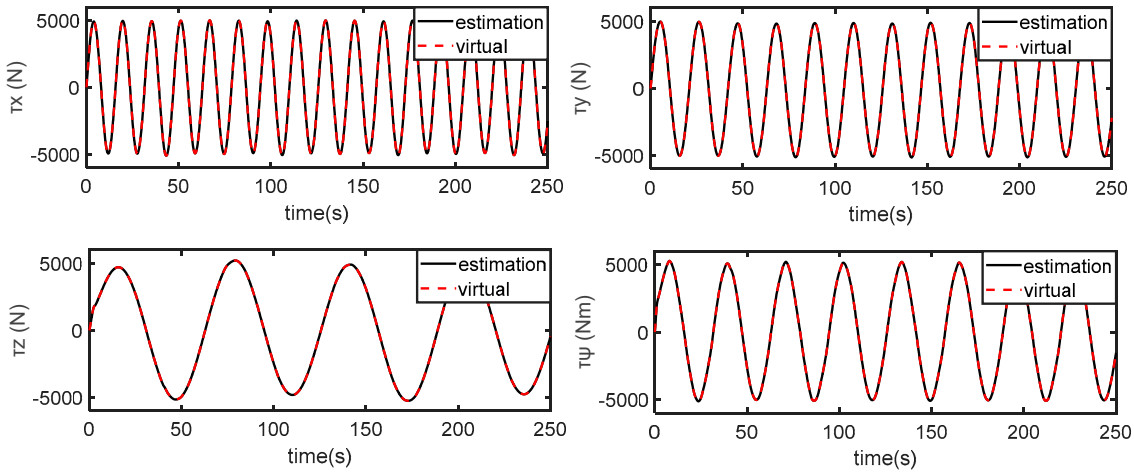

Figure 11. Observation of the lumped disturbance in simulation B.

5. Conclusions

In this article, an NDO-STDSMC method is proposed to deal with the problem of trajectory tracking control of ROVs with system uncertainties and external disturbances. This method utilizes a double-loop sliding-mode architecture. A novel controller is designed in the outer loop to improve the convergence rate. An inner-loop controller is designed to combine the advantages of the ST method and the NDO. In contrast to the DSMC scheme, the proposed method improves the robustness and tracking accuracy and results in a faster convergence rate. Additionally, the proposed method suppresses chattering while further improving the robustness compared with the STDSMC scheme. Rigid mathematical proofs are given for the proposed observer and controller. Two typical modes, ROVs with and without a TMS, are simulated. The simulation results prove that the proposed controller has advantages over the other two controllers in terms of control accuracy and robustness. Additionally, the proposed control scheme can effectively suppress chattering. In the future, we devote to constructing the pool experiment platform and engineering practice of the control methods mentioned in this paper to further verify the practical applicability of the proposed control scheme. In addition, the extension of NDO-STDSMC based on finite-time controller for ROVs with small delays will be presented in a future work.

Author Contributions: Conceptualization, B.H. and Q.Y.; methodology, B.H. and Q.Y.; software, B.H.; validation, B.H. and Q.Y.; formal analysis, B.H.; investigation, B.H.; resources, Q.Y.; data curation, B.H.; writing—original draft preparation, B.H.; writing—review and editing, Q.Y.; visualization, B.H.; supervision, Q.Y. All authors have read and agreed to the published version of the manuscript.

Funding: This research received no external funding.

Institutional Review Board Statement: Not applicable.

Informed Consent Statement: Not applicable.

Data Availability Statement: Not applicable.

Conflicts of Interest: The authors declare no conflict of interest.

Abbreviations

Disturbance observer	
$\hat{\boldsymbol{\tau}}_L$	the estimation of the disturbance
$\Im$	disturbance observer element
$\boldsymbol{K}(\boldsymbol{v}, \dot{\boldsymbol{v}})$	gain matrix of the observer
$\xi(\boldsymbol{v}, \dot{\boldsymbol{v}})$	auxiliary functions
δ	upper bound of the derivative
ϖ	positive constant
V_1	Lyapunov function of disturbance observer
Outer-loop controller	
$\boldsymbol{S}_w$	outer-loop sliding-mode surface
$\boldsymbol{\Gamma}_1$	gain vector of outer-loop sliding-mode surface
ρ_1	positive constant of outer-loop reaching law
k	positive constant of outer-loop reaching law
t_r	convergence time of outer-loop reaching law
V_2	Lyapunov function of outer-loop controller
Inner-loop controller	
$\boldsymbol{S}_n$	inner-loop sliding-mode surface
$\boldsymbol{\Gamma}_2$	gain vector of inner-loop sliding-mode surface
ρ_2, ρ_3	positive constant of inner-loop reaching law
$\Re_1$, $\Re_2$, σ_1, σ_2	auxiliary vectors of super-twisting method
$\boldsymbol{A}, \boldsymbol{B}, \gamma, \boldsymbol{P}$	auxiliary matrixes of super-twisting method
ω	positive constant
V_3	Lyapunov function of inner-loop controller

References

1. Schjølberg, I.; Utne, I.B. Towards autonomy in ROV operations. *IFAC Pap.* **2015**, *48*, 183–188. [CrossRef]
2. Zereik, E.; Bibuli, M.; Mišković, N.; Ridao, P.; Pascoal, A. Challenges and future trends in marine robotics. *Annu. Rev. Control* **2018**, *46*, 350–368. [CrossRef]
3. Yan, J.; Gao, J.; Yang, X.; Luo, X.; Guan, X. Position Tracking Control of Remotely Operated Underwater Vehicles with Communication Delay. *IEEE Trans. Control Syst. Technol.* **2019**, *28*, 2506–2514. [CrossRef]
4. Ippoliti, G.; Jetto, L.; Longhi, S. Improved set-points tracking of remotely operated underwater vehicles through a supervised PID control scheme. *J. Mar. Eng. Technol.* **2014**, *4*, 3–9. [CrossRef]
5. Shen, C.; Shi, Y.; Buckham, B. Trajectory Tracking Control of an Autonomous Underwater Vehicle Using Lyapunov-Based Model Predictive Control. *IEEE Trans. Ind. Electron.* **2018**, *65*, 5796–5805. [CrossRef]
6. Guerrero, J.; Torres, J.; Creuze, V.; Chemori, A. Trajectory tracking for autonomous underwater vehicle: An adaptive approach. *Ocean Eng.* **2019**, *172*, 511–522. [CrossRef]
7. Bessa, W.M.; Dutra, M.S.; Kreuzer, E. An adaptive fuzzy sliding mode controller for remotely operated underwater vehicles. *Robot. Auton. Syst.* **2010**, *58*, 16–26. [CrossRef]
8. Chu, Z.; Zhu, D.; Yang, S.X.; Jan, G.E. Adaptive Sliding Mode Control for Depth Trajectory Tracking of Remotely Operated Vehicle with Thruster Nonlinearity. *J. Navig.* **2016**, *70*, 149–164. [CrossRef]
9. Li, Z.; Yang, C.; Ding, N.; Bogdan, S.; Ge, T. Robust adaptive motion control for underwater remotely operated vehicles with velocity constraints. *Int. J. Control Autom. Syst.* **2012**, *10*, 421–429. [CrossRef]
10. Wang, Y.; Gu, L.; Gao, M.; Zhu, K. Multivariable Output Feedback Adaptive Terminal Sliding Mode Control for Underwater Vehicles. *Asian J. Control* **2016**, *18*, 247–265. [CrossRef]

11. Huang, B.; Yang, Q. Double-loop sliding mode controller with a novel switching term for the trajectory tracking of work-class ROVs. *Ocean Eng.* **2019**, *178*, 80–94. [CrossRef]
12. Garcia-Valdovinos, L.G.; Fonseca-Navarro, F.; Aizpuru-Zinkunegi, J.; Salgado-Jimenez, T.; Gomez-Espinosa, A.; Cruz-Ledesma, J.A. Neuro-Sliding Control for Underwater ROV's Subject to Unknown Disturbances. *Sensors* **2019**, *19*, 2943. [CrossRef]
13. Gao, J.; Zhang, G.; Wu, P.; Zhao, X.; Wang, T.; Yan, W. Model Predictive Visual Servoing of Fully-Actuated Underwater Vehicles with a Sliding Mode Disturbance Observer. *IEEE Access* **2019**, *7*, 25516–25526. [CrossRef]
14. Zhang, Y.; Liu, X.; Luo, M.; Yang, C. MPC-based 3-D trajectory tracking for an autonomous underwater vehicle with constraints in complex ocean environments. *Ocean Eng.* **2019**, *189*, 106309. [CrossRef]
15. Shen, C.; Buckham, B.; Shi, Y. Modified C/GMRES Algorithm for Fast Nonlinear Model Predictive Tracking Control of AUVs. *IEEE Trans. Control Syst. Technol.* **2017**, *25*, 1896–1904. [CrossRef]
16. Chu, Z.; Zhu, D.; Yang, S.X. Observer-Based Adaptive Neural Network Trajectory Tracking Control for Remotely Operated Vehicle. *IEEE Trans. Neural Netw. Learn. Syst.* **2017**, *28*, 1633–1645. [CrossRef]
17. Chu, Z.; Zhu, D.; Jan, G.E. Observer-based adaptive neural network control for a class of remotely operated vehicles. *Ocean Eng.* **2016**, *127*, 82–89. [CrossRef]
18. Shtessel, Y.; Taleb, M.; Plestan, F.J.A. A novel adaptive-gain supertwisting sliding mode controller: Methodology and application. *Automatica* **2012**, *48*, 759–769. [CrossRef]
19. Qiao, L.; Zhang, W. Adaptive Second-Order Fast Nonsingular Terminal Sliding Mode Tracking Control for Fully Actuated Autonomous Underwater Vehicles. *IEEE J. Ocean. Eng.* **2018**, *44*, 363–385. [CrossRef]
20. Guerrero, J.; Antonio, E.; Manzanilla, A.; Torres, J.; Lozano, R. Autonomous Underwater Vehicle Robust Path Tracking: Auto-Adjustable Gain High Order Sliding Mode Controller. *IFAC-Pap.* **2018**, *51*, 161–166. [CrossRef]
21. Joe, H.; Kim, M.; Yu, S.-C. Second-order sliding-mode controller for autonomous underwater vehicle in the presence of unknown disturbances. *Nonlinear Dyn.* **2014**, *78*, 183–196. [CrossRef]
22. Castañeda, H.; Salas-Peña, O.S.; de León-Morales, J. Extended observer based on adaptive second order sliding mode control for a fixed wing UAV. *ISA Trans.* **2017**, *66*, 226–232. [CrossRef]
23. Muñoz, F.; González-Hernández, I.; Salazar, S.; Espinoza, E.S.; Lozano, R. Second order sliding mode controllers for altitude control of a quadrotor UAS: Real-time implementation in outdoor environments. *Neurocomputing* **2017**, *233*, 61–71. [CrossRef]
24. Patel, K.; Mehta, A. Discrete-time Event-triggered Higher Order Sliding Mode Control for Consensus of 2-DOF Robotic Arms. *Eur. J. Control* **2020**, *56*, 231–241. [CrossRef]
25. Kali, Y.; Saad, M.; Benjelloun, K.; Fatemi, A. Discrete-time second order sliding mode with time delay control for uncertain robot manipulators. *Robot. Auton. Syst.* **2017**, *94*, 53–60. [CrossRef]
26. Muñoz-Vázquez, A.-J.; Ramírez-Rodríguez, H.; Parra-Vega, V.; Sánchez-Orta, A. Fractional sliding mode control of underwater ROVs subject to non-differentiable disturbances. *Int. J. Control Autom. Syst.* **2017**, *15*, 1314–1321. [CrossRef]
27. Fernandes, D.D.A.; Sørensen, A.J.; Pettersen, K.Y.; Donha, D.C. Output feedback motion control system for observation class ROVs based on a high-gain state observer: Theoretical and experimental results. *Control Eng. Pract.* **2015**, *39*, 90–102. [CrossRef]
28. Hernandez-Alvarado, R.; Garcia-Valdovinos, L.G.; Salgado-Jimenez, T.; Gomez-Espinosa, A.; Fonseca-Navarro, F. Neural Network-Based Self-Tuning PID Control for Underwater Vehicles. *Sensors* **2016**, *16*, 1429. [CrossRef] [PubMed]
29. Chen, M.; Chen, W.-H. Sliding mode control for a class of uncertain nonlinear system based on disturbance observer. *Int. J. Adapt. Control Signal Process.* **2009**, *24*, 51–64. [CrossRef]
30. Patre, B.M.; Londhe, P.S.; Waghmare, L.M.; Mohan, S. Disturbance estimator based non-singular fast fuzzy terminal sliding mode control of an autonomous underwater vehicle. *Ocean Eng.* **2018**, *159*, 372–387. [CrossRef]
31. Wu, J.; Huang, J.; Wang, Y.; Xing, K. Nonlinear Disturbance Observer-Based Dynamic Surface Control for Trajectory Tracking of Pneumatic Muscle System. *IEEE Trans. Control Syst. Technol.* **2014**, *22*, 440–455. [CrossRef]
32. Qiao, L.; Zhang, W. Double-Loop Integral Terminal Sliding Mode Tracking Control for UUVs with Adaptive Dynamic Compensation of Uncertainties and Disturbances. *IEEE J. Ocean. Eng.* **2018**, *44*, 29–53. [CrossRef]
33. Li, J.; Guo, H.; Zhang, H.; Yan, Z. Double-Loop Structure Integral Sliding Mode Control for UUV Trajectory Tracking. *IEEE Access* **2019**, *7*, 101620–101632. [CrossRef]
34. Wadi, A.; Mukhopadhyay, S.; Lee, J.-H. A novel disturbance-robust adaptive trajectory tracking controller for a class of underactuated autonomous underwater vehicles. *Ocean Eng.* **2019**, *189*, 106377. [CrossRef]
35. Yan, Z.; Wang, M.; Xu, J. Robust adaptive sliding mode control of underactuated autonomous underwater vehicles with uncertain dynamics. *Ocean Eng.* **2019**, *173*, 802–809. [CrossRef]
36. Pérez-Ventura, U.; Fridman, L. Design of super-twisting control gains: A describing function based methodology. *Automatica* **2019**, *99*, 175–180. [CrossRef]
37. Ioannou, P.A.; Sun, J. *Robust Adaptive Control*; PTR Prentice-Hall: Upper Saddle River, NJ, USA, 1996; Volume 1.
38. Li, X.; Zhao, M.; Ge, T. A Nonlinear Observer for Remotely Operated Vehicles with Cable Effect in Ocean Currents. *Appl. Sci.* **2018**, *8*, 867. [CrossRef]
39. Luo, Y.; Wu, M.; Wang, Z.; Wang, Z. Multivariable Robust Fault Tolerant Control for Work-Class Remotely Operated Vehicle. *Period. Polytech. Mech. Eng.* **2017**, *61*, 87–93.